Magnetic microcalorimeter with paramagnetic temperature sensors and integrated dc-SQUID readout for high-resolution x-ray emission spectroscopy EP

Matthäus Krantz ; Francesco Toschi ; Benedikt Maier ; Greta Heine; Christian Enss ; Sebastian Kempf ✉

Check for updates

View Online

Export Citation

17 December 2024 10:59:53

Magnetic microcalorimeter with paramagnetic temperature sensors and integrated dc-SQUID readout for high-resolution x-ray emission spectroscopy EP

Matthäus Krantz,[1] (iD) Francesco Toschi,[2,3] (iD) Benedikt Maier,[4] (iD) Greta Heine,[4] Christian Enss,[3,5] (iD) and Sebastian Kempf[3,6,a)] (iD)

AFFILIATIONS

[1]Kirchhoff-Institute for Physics, Heidelberg University, Im Neuenheimer Feld 227, 69120 Heidelberg, Germany

[2]Institute for Astroparticle Physics (IAP), Karlsruhe Institute of Technology (KIT), Hermann-von-Helmholtz-Platz 1, 76344 Eggenstein-Leopoldshafen, Germany

[3]Kirchhoff-Institute for Physics (KIP), Heidelberg University, Im Neuenheimer Feld 227, 69120 Heidelberg, Germany

[4]Institute of Experimental Particle Physics (ETP), Karlsruhe Institute of Technology (KIT), Wolfgang-Gaede-Str. 1, 76131 Karlsruhe, Germany

[5]Institute for Data Processing and Electronics (IPE), Karlsruhe Institute of Technology (KIT), Hermann-von-Helmholtz-Platz 1, 76344 Eggenstein-Leopoldshafen, Germany

[6]Institute of Micro- and Nanoelectronic Systems, Karlsruhe Institute of Technology, Hertzstraße 16, 76187 Karlsruhe, Germany

[a)]Author to whom correspondence should be addressed: sebastian.kempf@kit.edu

ABSTRACT

We present two variants of a magnetic microcalorimeter with paramagnetic temperature sensors and integrated dc-superconducting quantum interference device readout for high-resolution x-ray emission spectroscopy. Each variant employs two overhanging gold absorbers with a sensitive area of $150 \times 150\,\mu m^2$ and a thickness of $3\,\mu m$, thus providing a thickness related quantum efficiency of $>98\%$ for photons up to $5\,keV$ and $>50\%$ for photons up to $10\,keV$. The first variant operated nominally but suffered from Joule power dissipation of the Josephson junction shunt resistors, athermal phonon loss, and slew rate limitations of the overall setup. Overall, it only achieved an energy resolution of $\Delta E_{FWHM} = 8.9\,eV$ for $5.9\,keV$ photons. In the second variant, we introduced an innovative tetrapod absorber geometry as well as a membrane technique for diverting dissipated heat away from the temperature sensors. When all mitigations are applied optimally, the second variant achieves an energy resolution of $\Delta E_{FWHM} = 1.25(18)\,eV$ for $5.9\,keV$ photons and hence provides the present best energy resolving power $E/\Delta E_{FWHM}$ among all existing energy-dispersive detectors for soft and tender x-rays.

X-ray emission spectroscopy (XES) is an exceptionally powerful tool to study fundamental properties of materials such as chemical states or atomic and electronic structure of constituents.[1,2] By analyzing the x-ray photons, which are emitted by the sample, it provides valuable information that would be challenging using other techniques. However, to exploit its full power, an x-ray detector with demanding properties is required. Important figures of merit are energy resolution, detection efficiency as set by photon absorption efficiency and solid angle coverage, throughput, count rate capability as well as granularity,

i.e., the number of pixels within the sensitive detection area. In this respect, cryogenic microcalorimeters, such as superconducting transition-edge sensors (TESs)[3–5] or magnetic microcalorimeters (MMCs),[6,7] are striking detector technologies as they combine an excellent energy resolution, a large dynamic range, and a quantum efficiency close to 100% in a single device.[2,5,8] Moreover, they can be arranged in densely packed detector arrays and hence allow to yield a high detection efficiency as well as a suitable count rate. Using an ultra-sensitive thermometer, based on either superconducting (TESs)

or paramagnetic (MMCs) materials, as well as an appropriate readout circuit, cryogenic microcalorimeters convert the energy input into a change of current or magnetic flux, respectively, that can be sensed using superconducting quantum interference devices (SQUIDs). Existing microcalorimeters achieved an energy resolution ΔE_{FWHM} of 0.72 eV for 1.5 keV photons[9] and 1.6 eV for 5.9 keV photons.[7,10] This corresponds to an energy resolving power $E/\Delta E_{\mathrm{FWHM}}$ of ~ 2100 and ~ 3700, respectively.

Among the existing cryogenic detectors, magnetic microcalorimeters stand out in the sense that they simultaneously provide an excellent energy resolution, an intrinsically fast signal rise time, a huge dynamic range, as well as easy calibration and excellent linearity.[7] However, at the same time, they are susceptible to SQUID noise that easily can limit the achievable energy resolution.[7] One possibility to deal with this challenge is to integrate the temperature sensor(s) directly into the SQUID loop.[7,11,12] However, the close vicinity between the resistive junction shunts and the temperature sensors makes such devices rather sensitive to SQUID Joule power dissipation and has hampered the usage of such devices in the past. Nonetheless, we revisited this old idea and now present two variants of a magnetic microcalorimeter with paramagnetic temperature sensors and integrated dc-SQUID readout for high-resolution x-ray emission spectroscopy. While the first variant turned out to be susceptible to power dissipation caused by the junction shunts, we included countermeasures in our second variant. By this, the second variant achieves an energy resolution of $\Delta E_{\mathrm{FWHM}} = 1.25(18)$ eV for 5.9 keV photons and hence provides the present best energy resolving power $E/\Delta E_{\mathrm{FWHM}}$ among all existing energy-dispersive detectors for soft and tender x-rays. Combined with a state-of-the-art multiplexing technique to implement large-scale detector arrays, the second detector variant could be used, for example, for performing *in situ* or *in-operando* studies of radiation sensitive of highly diluted samples at modern synchrotron or even laboratory x-ray light sources.[2]

Figure 1 shows a colorized scanning electron microscope (SEM) picture, an exploded-view drawing, a simplified layout drawing as well

as a microscope photograph of the first variant of our microcalorimeter. The main SQUID loop is based on two superconducting meander-shaped coils made of Nb that are connected in parallel to the Josephson junctions to form a first-order parallel-gradiometer. The pitch and linewidth of each coil are $p_2 = 10\,\mu m$ and $w_2 = 4\,\mu m$, respectively. Underneath the SQUID loop, a meander-shaped coil is running essentially replicating the shape of the main SQUID loop. The pitch and linewidth of this coil are $p_1 = 10\,\mu m$ and $w_1 = 6\,\mu m$, respectively. The linewidth w_1 is chosen slightly larger than that of the SQUID loop to account for the alignment accuracy of our fabrication equipment. This "field coil" is used for generating the bias magnetic field required to magnetize the temperature sensors. For this, a persistent current is injected into the coil using a resistive persistent current switch that is located nearby the SQUID loop. It is worth mentioning that separating field and pickup coil allows simultaneously injecting a persistent current into several microcalorimeters by serially connecting all field coils. In case only one coil would be used, the ground connection of the SQUID forms as parasitic current path hampering a reliable persistent current injection. We additionally note that the coil arrangement is gradiometric in nature, i.e., the magnetic field generated by the field coil is not causing a noticeable flux bias of the SQUID that could potentially cause a negative effect of the dynamic range or other SQUID properties.

The window-type Josephson junctions are made from an Nb/Al-AlO$_x$/Nb trilayer and have a target critical current of $I_c \approx 6.3\,\mu A$. Each junction is shunted by a resistor with $R_s \approx 5\,\Omega$ made of Au:Pd that is connected to a cooling fin. To increase its effective volume, the shunt resistor is covered with a sputtered Au layer that does not affect the shunt resistance. To dampen parasitic resonances in the *IV*-characteristic of the SQUID, we connected a resistor with $R_s = 10\,\Omega$ in parallel to the SQUID loop. The SQUID loop is inductively coupled to a feedback coil for flux-biasing as well as flux-locked loop operation.

A Ag:Er temperature sensor with an area of $50 \times 50\,\mu m^2$ is placed on top of the meander-shaped SQUID loop using a liftoff
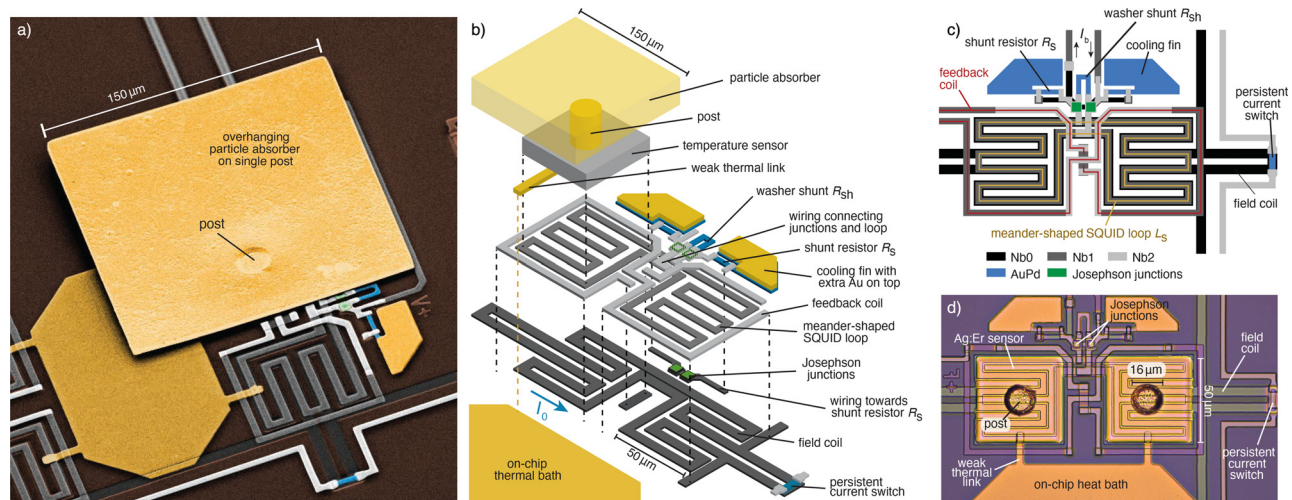
FIG. 1. (a) Colorized SEM picture, (b) exploded-view drawing, (c) simplified layout drawing, and (d) microscope photograph of the first variant of our microcalorimeter with paramagnetic temperature sensors and integrated dc-SQUID readout. For visibility, we show images where we omitted or removed one or two absorbers and/or temperature sensors. For the same reason, the layout drawing in (c) only shows the arrangement of the three Nb layers, the Josephson tunnel junctions as well as the resistive Au:Pd structures.

technique. For the first detector variant, the Er concentration and sensor height are 450 ppm and 1.2 μm, respectively. Based on the measured detector response and noise characteristics of this first detector, the second detector variant has an Er concentration of 260 ppm and a sensor width of 0.8 μm. For changing the concentration, a new sputter target was built. The overhanging particle absorbers are made of electroplated gold with dimensions of $150 \times 150 \times 3 \mu m^3$, resulting in a heat capacity of each absorber of $C_{abs} = 0.1$ pJ/K at $T = 20$ mK. A single post with a diameter of $d = 16 \mu$m connects the absorber with the underlying temperature sensor. The cross-sectional area of the stem is about 8% of the total sensor area and is, hence, rather large as compared to other MMCs.[13] The aim of this post is to avoid athermal phonon loss during the initial phase of detector thermalization.[14] Although the stem diameter should be generally as small as possible,[10,13–15] we found that for the given absorber geometry (size and thickness) a single post with a rather large diameter is structurally much more stable than several posts with a smaller stem diameter.

For device characterization, we mounted a prototype device into a ^{3}He/^{4}He dilution refrigerator using a custom-made sample holder. The latter was designed to allow the screening of the detector against external magnetic field fluctuations using a superconducting Al shield as well as the operation of the detector in a two-stage dc-SQUID configuration with voltage bias and flux-locked loop. We used an updated version of our home-made 16-dc-SQUID series arrays[16] as a low-noise amplifier SQUID as well as a directly coupled, high-speed, room-temperature SQUID readout electronics with a FLL-bandwidth of 6 MHz[17] that was used for all measurements reported below. We irradiated the detector with x-rays emitted by an ^{55}Fe calibration source mounted inside the cryostat.

Figure 2 shows a summary of the most important findings of the characterization of the first detector variant. The detector was fully functional, despite the very high complexity of its manufacture that includes fourteen different photolithographic layers including three independent Nb layers. We achieved an energy resolution of $\Delta E_{FWHM} = 8.9$ eV being about an order of magnitude worse than our

expectation. After careful investigation/analysis, we found the SQUID Joule heating to be the main source of the performance degradation. When biasing the detector to yield optimum noise performance (high bias), the temperature sensors being located nearby the shunt resistors did not go below $T \approx 65$ mK. In contrast, when biasing the SQUID with the smallest possible bias voltage to yield the largest detector signals (low bias), the overall noise level was more than a factor of three higher than under high bias conditions. Moreover, the deviation between the measured and predicted signal size indicated that even for the smallest bias voltage the signal height was about a factor of two smaller than possible. Additionally, we found that the detector suffered slightly from athermal phonon loss due to the rather large fraction between the stem and sensor area as well as strongly from hitting the slew rate limit of the SQUID setup that was determined by the length of the wiring as well as the total SQUID gain. The latter became noticeable by a linear rather than exponential dependence of the time course of the signal rise [see Fig. 2(c)].

We investigated several methods to reduce the impact of SQUID Joule heating, athermal phonon loss, and slew rate limitation on the detector performance. We resolved the latter two by introducing a tetrapod absorber geometry as depicted in Fig. 3. Here, the particle absorber is not directly attached to the temperature sensor, but instead on top of a four-legged bridge (tetrapod). In this geometry, the direct line of sight between absorber and sensor has a smaller cross-sectional area, significantly reducing the probability for athermal phonons to escape. We placed one tetrapod leg on top of a thermal link made of sputtered gold. By varying the length and width of this link, we can set the signal rise time. We empirically determined that the detector rise is exponential (and hence not slew rate limited) as soon as the rise time is down to about ~10 μs. Though this slowdown impacts the time resolution of the detector, the energy resolution is not affected as the effective bandwidth of the detector is smaller.[18] Nevertheless, we note that this mitigation step impacts one of the main advantages of magnetic microcalorimeters, i.e., the intrinsic fast signal rise time. For this reason, we will investigate in detail whether we have approached a
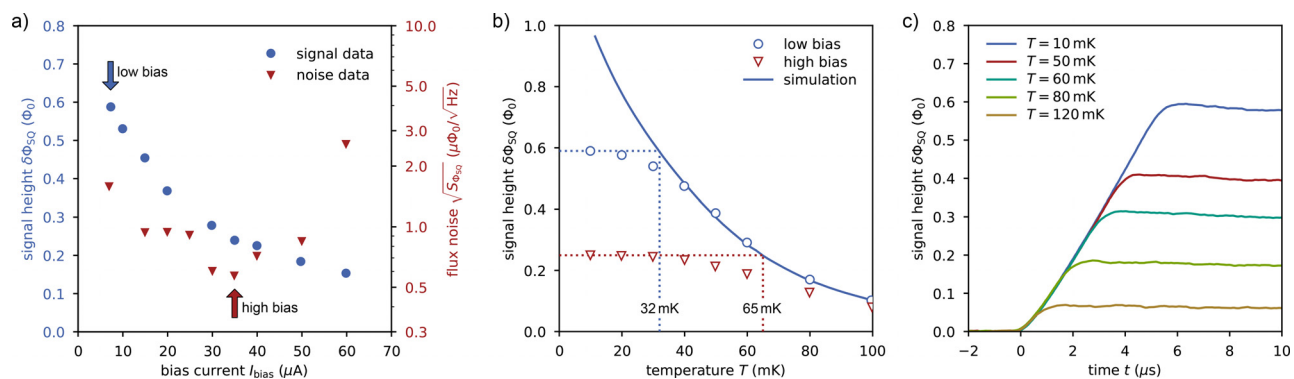

FIG. 2. (a) Signal height $\delta\Phi_{SQ}$ for an energy input of 5.9 keV and white noise level $\sqrt{S_{\Phi_{SQ}}}$ vs bias current I_{bias} used for creating the voltage bias of the detector within a two-stage dc-SQUID configuration. The measurement was performed at cryostat base temperature ($T \simeq 7$ mK). The arrows indicate the bias currents that are referenced in the middle plot. (b) Signal height $\delta\Phi_{SQ}$ vs heat bath temperature T when biasing the SQUID with smallest possible bias voltage to achieve the largest detector signals (low bias) as well as when biasing the detector to yield optimum noise performance (high bias). In addition, we show the simulated dependence for the given operation and detector parameters. The deviation between measurement and simulation toward low temperatures is caused by a thermal decoupling of the detector from the heat bath due to SQUID Joule heating. The dashed lines are extrapolation from the measured data to the expected values and allow determining the actual detector temperature. (c) Signal height $\delta\Phi_{SQ}$ vs time t for detector signals of different heights.
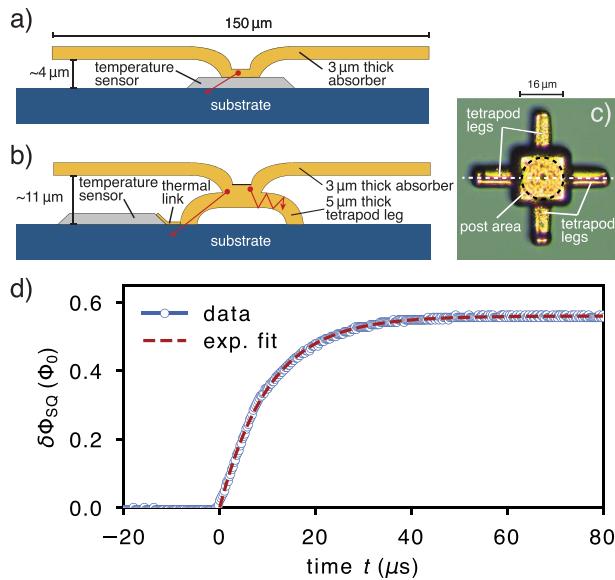
FIG. 3. Illustration of the (a) conventional and (b) tetrapod absorber geometry. The red arrows show possible traveling paths for athermal phonons generated within the absorber. In the conventional geometry, athermal phonons can easily escape to the substrate, while in the tetrapod geometry, the cross-sectional area of direct line of sight is reduced. (c) Microscope picture of a finalized tetrapod structure on a test sample. To view the actual tetrapod, the particle absorber that is connected via an electroplated post at the post area has been omitted for the test sample. The dashed line indicates the view along the tetrapod that is shown in (b). (d) Time course of the signal rise of the final prototype detector of the second variant. The red dashed line shows an exponential fit to the measured detector response. The extracted rise time (time constant of the exponential fit function) is 10 μs.

fundamental limitation in SQUID design or whether a larger slew rate can be achieved without affecting SQUID noise or degrading the detector sensitivity.

For reducing the impact of SQUID Joule heating, we investigated several methods, among which a reduction of the shunt resistance as well as backside coating of the detector with a 1 μm thick Au layer. The latter acts as a sink for athermal phonons emitted by the shunts and ballistically traversing through the silicon substrate, and it enhances the thermal coupling between detector and sample holder. In combination, both techniques allowed to lower the actual detector temperature to 25 mK, even when using a bias minimizing the SQUID noise. This greatly improved the detector performance, and we achieved an energy resolution as low as $\Delta E_{FWHM} \simeq 2.4$ eV. Nevertheless, we noticed that the detector performance still remains susceptible to the number of detectors operated within an array. For this reason, we developed a method that is based on placing the shunt resistors on a thin SiO_2 membrane[20] and to thermally anchor the shunts through a separate metallic link directly to the sample holder. Figure 4 shows several illustrations of this method and indicates that field coil, SQUID loop, and both temperature sensors and absorbers are placed on the solid substrate. The shunt resistors are still connected to a cooling fin. Below the shunt resistors, the Si substrate is removed by isotropic reactive ion etching. The shunts are, hence, hovering on a membrane formed by the 240 nm thick thermal SiO_2 electrically insulating the Si wafer. As the SiO_2 membrane is rather fragile, we used Nb beams to stabilize the membrane. Overall, the

SiO_2 membrane greatly reduces the thermal conductance between the shunt resistors and the temperature sensors and prohibits that dissipated energy is transferred into the solid substrate. To sink the heat generated by the junction shunts, we provide a separate thermalization pathway to the sample holder by electro-depositing an Au thermalization link on top of the cooling fin as well as on a small part of the solid substrate for structural stability. This thermalization link is coupled to the sample holder via Au wire bonds. Since at MMC operation temperatures, the phononic thermal conductance is orders of magnitude lower than the electronic one as well as due to the Kapitza resistance, only a negligible fraction of the dissipated energy is transferred from the Au thermalization link into the Si substrate. Overall, the separation of the shunt resistors from the temperature sensors made it possible to greatly reduce the impact of the SQUID Joule heating on the detector performance and to lower the actual sensor temperature to about 17 mK [see Fig. 5(a)]. We can hence use an optimal SQUID bias to get very low SQUID noise and large signals. Moreover, we noticed that we are only missing about 20% of signal size as compared to our detector simulations [see Fig. 5(a)]. The remaining thermal decoupling of the temperature sensors from the heat bath is likely caused by the washer shunt of the SQUID that is not sitting on the SiO_2 membrane as well as the fact that we potentially loose some heat to the Si substrate via the thermalization links. Both points can be addressed in a future design by placing the washer shunt on the membrane as well as using normal-conducting through-silicon vertical interconnects (vias) for heat sinking of the shunt resistors on the membrane.

Figures 5(b) and 5(c) show the energy spectra of the K_{α} and K_{β} line of the ^{55}Fe calibration source as acquired with the latest prototype detector of the second detector variant that uses the tetrapod absorber geometry with a signal rise time of about 10 μs as well as a SiO_2 membrane to thermally separate the temperature sensors from the shunt resistors. For the analysis of the acquired signals, we used an optimal filter technique that is described in detail in a separate publication.[19] During analysis, we found that the detector is affected by strong drifts of the heat bath temperature that was not regulated during the measurement as the temperature controller induced severe disturbances to the detector. To (partially) account for the resulting degradation of energy resolution, we performed a temperature correction of the signal heights and excluded the signals with largest temperature deviations. In total, 26% of all acquired physical/good signals were discarded. Moreover, we assumed that the detector response is generally Gaussian, but can be potentially affected by athermal phonon loss leading to a low energy tail of the spectra. By performing a sophisticated fitting procedure[19] and minimizing the χ^2-deviation between the measured spectrum and the detector model, we find that athermal phonon loss is negligible and that the energy resolution of the detector is $\Delta E_{FWHM} = 1.25(18)$ eV when excluding the detector signals with largest temperature deviations. When accepting all detector signals (and including athermal phonon loss), the energy resolution is $\Delta E_{FWHM} = 1.35(17)$ eV.[21] The baseline resolution, i.e., the energy resolution of hypothetical detector events with 0 eV energy deposition, is $\Delta E_{FWHM} = 1.1$ eV and is, hence, very close to the measured energy resolution at 5.9 keV. This shows that the signal gain of the detector is virtually constant over the entire soft and tender x-ray energy range. The expected energy resolution at the effective detector operation temperature, i.e., $T \approx 18$ mK, is 0.64 eV and deviates by about a factor of two from the achieved value. We presently attribute this to the
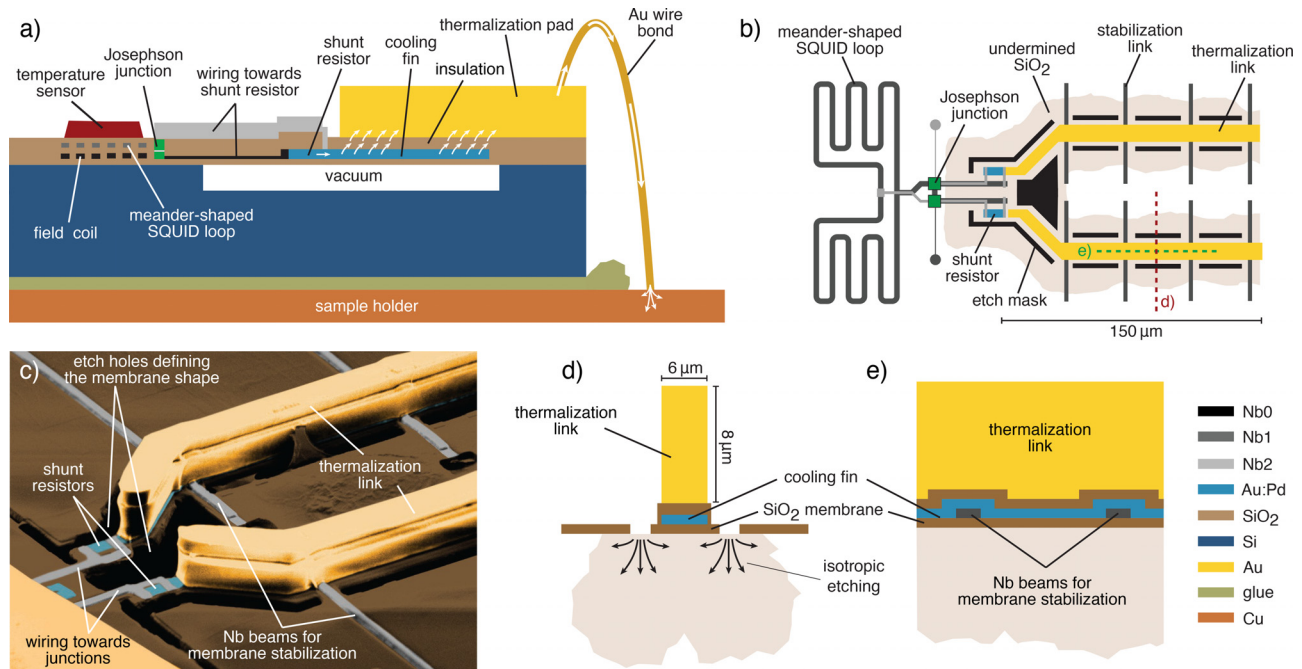
FIG. 4. Schematic illustration of a (a) side view and (b) top view of the membrane arrangement developed to reduce the impact of SQUID Joule heating on the detector performance. (c) Colorized SEM picture of the shunt resistor section of a finalized prototype detector of the second variant. The thermalization bridges and stabilization structures are sitting on a SiO$_2$ membrane that is undermined using SF$_6$ based reactive ion etching. (d) and (e) Cross-sectional views of the regions marked in (b).

substantial temperature fluctuations of the mixing chamber platform (and hence the detector setup) that were as large as $\Delta T/T \simeq 6.4 \times 10^{-4}$ (measured with the mixing chamber thermometer). As a result, we plan to improve the temperature stability of our cryostat and subsequently to systematically study whether sub-eV energy resolution can be achieved or whether we are approaching a yet unknown limit. Despite this remaining point, we nonetheless note that the presented

detector provides the best energy resolution power $E/\Delta E_{\mathrm{FWHM}}$ of any energy-dispersive detector in the soft and tender x-ray range.

In conclusion, we have presented two variants of a magnetic microcalorimeter with paramagnetic temperature sensors and integrated dc-SQUID readout for high-resolution x-ray emission spectroscopy. As the first variant suffers from Joule power dissipation of the SQUID, athermal phonon loss, and reaching the slew rate limit of the
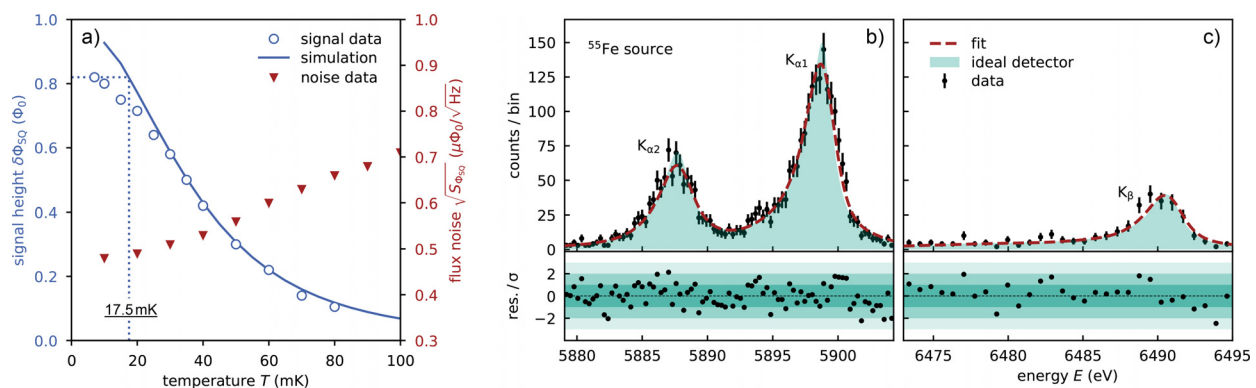

FIG. 5. (a) Signal height $\delta\Phi_{\mathrm{SQ}}$ for an energy input of 5.9 keV and white noise level $\sqrt{S_{\Phi_{\mathrm{SQ}}}}$ vs temperature T as well as the expected dependence derived by numerically simulating the detector behavior. The deviation of the measured data from the simulation toward low temperatures is caused by a slight thermal decoupling of the detector from the heat bath due to remaining SQUID power dissipation. The dashed line is an extrapolation from the measured data to the expected values from which we can determine the actual detector temperature. (b) K_α and (c) K_β line of the ^{55}Fe calibration source used for detector characterization. The solid red lines are the result of a fitting procedure to determine the energy resolution $\Delta E_{\mathrm{FWHM}} = 1.25(18)$ eV of the detector. The filled areas illustrate the shape of the expected spectra assuming an ideal detector with $\Delta E_{\mathrm{FWHM}} = 0$ eV. Comprehensive details about the data analysis and a breakdown of the statistical and systematic errors are discussed by Toschi et al.[19]

overall setup, we introduced a tetrapod absorber geometry as well as a membrane technique. By this, the detector achieves an energy resolution of $\Delta E_{\mathrm{FWHM}} = 1.25(18)\,\mathrm{eV}$ for 5.9 keV photons and hence provides the best energy resolving power among all existing energy-dispersive x-ray detectors in the soft and tender x-ray range.

AUTHOR DECLARATIONS
Conflict of Interest

The authors have no conflicts to disclose.

Author Contributions

Matthäus Krantz: Conceptualization (equal); Formal analysis (equal); Investigation (lead); Visualization (lead); Writing – original draft (supporting); Writing – review & editing (equal). **Francesco Toschi:** Formal analysis (lead); Software (equal); Writing – review & editing (equal). **Benedikt Maier:** Formal analysis (equal); Software (equal); Writing – review & editing (equal). **Greta Heine:** Formal analysis (equal); Software (equal); Writing – review & editing (equal). **Christian Enss:** Conceptualization (supporting); Funding acquisition (lead); Investigation (equal); Project administration (supporting); Resources (lead); Supervision (equal); Writing – review & editing (equal). **Sebastian Kempf:** Conceptualization (equal); Formal analysis (supporting); Investigation (equal); Project administration (supporting); Resources (equal); Supervision (equal); Visualization (equal); Writing – original draft (lead); Writing – review & editing (equal).

DATA AVAILABILITY

The data that support the findings of this study are available from the corresponding author upon reasonable request.

REFERENCES

[1] F. de Groot, "High-resolution X-ray emission and X-ray absorption spectroscopy," Chem. Rev. **101**, 1779–1808 (2001).

[2] J. Uhlig, W. B. Doriese, J. W. Fowler, D. S. Swetz, C. Jaye, D. A. Fischer, C. D. Reintsema, D. A. Bennett, L. R. Vale, U. Mandal, G. C. O'Neil, L. Miaja-Avila, Y. I. Joe, A. El Nahhas, W. Fullagar, F. P. Gustafsson, V. Sundstrom, D. Kurunthu, G. C. Hilton, D. R. Schmidt, and J. N. Ullom, "High-resolution X-ray emission spectroscopy with transition-edge sensors: Present performance and future potential," J. Synchrotron Radiat. **22**, 766–775 (2015).

[3] K. Irwin and G. Hilton, "Transition-edge sensors," in *Cryogenic Particle Detection*, edited by C. Enss (Springer, Berlin Heidelberg, 2005), pp. 63–150.

[4] J. N. Ullom and D. A. Bennett, "Review of superconducting transition-edge sensors for x-ray and gamma-ray spectroscopy," Supercond. Sci. Technol. **28**, 084003 (2015).

[5] S. Friedrich, "Cryogenic X-ray detectors for synchrotron science," J. Synchrotron Radiat. **13**, 159–171 (2006).

[6] A. Fleischmann, C. Enss, and G. Seidel, "Metallic magnetic calorimeters," in *Cryogenic Particle Detection*, edited by C. Enss (Springer, Berlin Heidelberg, 2005), pp. 151–216.

[7] S. Kempf, A. Fleischmann, L. Gastaldo, and C. Enss, "Physics and applications of metallic magnetic calorimeters," J. Low Temp. Phys. **193**, 365–379 (2018).

[8] W. B. Doriese, P. Abbamonte, B. K. Alpert, D. A. Bennett, E. V. Denison, Y. Fang, D. A. Fischer, C. P. Fitzgerald, J. W. Fowler, J. D. Gard, J. P. Hays-Wehle, G. C. Hilton, C. Jaye, J. L. McChesney, L. Miaja-Avila, K. M. Morgan, Y. I. Joe, G. C. O'Neil, C. D. Reintsema, F. Rodolakis, D. R. Schmidt, H. Tatsuno, J. Uhlig, L. R. Vale, J. N. Ullom, and D. S. Swetz, "A practical superconducting-microcalorimeter X-ray spectrometer for beamline and laboratory science," Rev. Sci. Instrum. **88**, 053108 (2017).

[9] S. J. Lee, J. S. Adams, S. R. Bandler, J. A. Chervenak, M. E. Eckart, F. M. Finkbeiner, R. L. Kelley, C. A. Kilbourne, F. S. Porter, J. E. Sadleir, S. J. Smith, and E. J. Wassell, "Fine pitch transition-edge sensor X-ray microcalorimeters with sub-eV energy resolution at 1.5 keV," Appl. Phys. Lett. **107**, 223503 (2015).

[10] S. J. Smith, J. S. Adams, C. N. Bailey, S. R. Bandler, J. A. Chervenak, M. E. Eckart, F. M. Finkbeiner, R. L. Kelley, C. A. Kilbourne, F. S. Porter, and J. E. Sadleir, "Small pitch transition-edge sensors with broadband high spectral resolution for solar physics," J. Low Temp. Phys. **167**, 168–175 (2012).

[11] V. Zakosarenko, R. Stolz, L. Fritzsch, H. G. Meyer, A. Fleischmann, and C. Enns, "SQUID gradiometer for ultra-low temperature magnetic micro-calorimeter," Supercond. Sci. Technol. **16**, 1404–1407 (2003).

[12] R. Stolz, V. Zakosarenko, L. Fritzsch, H. G. Meyer, A. Fleischmann, and C. Enns, "SQUID-gradiometers for arrays of integrated low temperature magnetic micro-calorimeters," IEEE Trans. Appl. Supercond. **15**, 773–776 (2005).

[13] A. Fleischmann, L. Gastaldo, S. Kempf, A. Kirsch, A. Pabinger, C. Pies, J. P. Porst, P. Ranitzsch, S. Schäfer, F. Seggern, T. Wolf, C. Enns, and G. M. Seidel, "Metallic magnetic calorimeters," AIP Conf. Proc. **1185**, 571–578 (2009).

[14] A. G. Kozorezov, C. J. Lambert, S. R. Bandler, M. A. Balvin, S. E. Busch, P. N. Nagler, J.-P. Porst, S. J. Smith, T. R. Stevenson, and J. E. Sadleir, "Athermal energy loss from x-rays deposited in thin superconducting films on solid substrates," Phys. Rev. B **87**, 104504 (2013).

[15] A. M. Datesman, J. S. Adams, S. R. Bandler, G. L. Betancourt-Martinez, M.-P. Chang, J. A. Chervenak, M. E. Eckart, A. E. Ewin, F. M. Finkbeiner, J. Y. Ha, R. L. Kelley, C. A. Kilbourne, A. R. Miniussi, F. S. Porter, J. E. Sadleir, K. Sakai, S. J. Smith, N. A. Wakeham, E. H. Williams, E. J. Wassell, and W. Yoon, "Reduced-scale transition-edge sensor detectors for solar and X-ray astrophysics," IEEE Trans. Appl. Supercond. **27**, 2100505 (2017).

[16] S. Kempf, A. Ferring, A. Fleischmann, and C. Enns, "Direct-current superconducting quantum interference devices for the readout of metallic magnetic calorimeters," Supercond. Sci. Technol. **28**, 045008 (2015).

[17] D. Drung, C. Hinnrichs, and H.-J. Barthelmess, "Low-noise ultra-high-speed dc SQUID readout electronics," Supercond. Sci. Technol. **19**, S235–S241 (2006).

[18] S. R. Bandler, K. D. Irwin, D. Kelly, P. N. Nagler, J. P. Porst, H. Rotzinger, J. E. Sadleir, G. M. Seidel, S. J. Smith, and T. R. Stevenson, "Magnetically coupled microcalorimeters," J. Low Temp. Phys. **167**, 254–268 (2012).

[19] F. Toschi, B. Maier, G. Heine, T. Ferber, S. Kempf, M. Klute, and B. V. Krosigk, "Optimum filter-based analysis for the characterization of a high-resolution magnetic microcalorimeter towards the DELight experiment," arXiv:2310.08512 (2023).

[20] We used our standard thermally oxidized Si wafers for fabricating the detector. For future fabrications runs, we might investigate whether Si wafers coated with low-stress Si_3N_4 might simplify the fabrications and enhance the reliability and quality.

[21] We note that the quoted errors contain both the statistical and systematic errors and refer to Toschi *et al.*[19] for a comprehensive breakdown of different error contributions.